

PROCEEDINGS OF SPIE

SPIDigitalLibrary.org/conference-proceedings-of-spie

Multiscale photoacoustic tomography of a genetically encoded near-infrared FRET biosensor

Li, Lei, Wang, Lihong, Verkhusha, Vladislav, Shcherbakova, Daria

Lei Li, Lihong Wang, Vladislav V. Verkhusha, Daria Shcherbakova, "Multiscale photoacoustic tomography of a genetically encoded near-infrared FRET biosensor," Proc. SPIE 11960, Photons Plus Ultrasound: Imaging and Sensing 2022, 119600J (3 March 2022); doi: 10.1117/12.2610587

SPIE.

Event: SPIE BiOS, 2022, San Francisco, California, United States

Multiscale photoacoustic tomography of a genetically encoded near-infrared FRET biosensor

Lei Li¹, Vladislav V. Verkhusha², Daria M. Shcherbakova², and Lihong V. Wang^{1*}

¹Caltech Optical Imaging Laboratory, Andrew and Peggy Cherng Department of Medical Engineering and Department of Electrical Engineering, California Institute of Technology, Pasadena, CA 91125, USA;

²Department of Anatomy and Structural Biology, and Gruss-Lipper Biophotonics Center, Albert Einstein College of Medicine, Bronx, NY 10461, USA

* Correspondence should be addressed to: L.V.W. (LVW@caltech.edu)

ABSTRACT

Photoacoustic tomography (PAT) with genetically encoded near-infrared probes enables visualization of specific cell populations *in vivo* at high resolution deeply in biological tissues. However, because of a lack of proper probes, PAT of cellular dynamics remains unexplored. Here, we report a near-infrared Förster resonance energy transfer (FRET) biosensor based on a miRFP670-iRFP720 pair of the near-infrared fluorescent proteins, which enables dynamic functional imaging of active biological processes in deep tissues. By photoacoustically detecting the changes in optical absorption of the miRFP670 FRET-donor, we monitored cell apoptosis in deep tissue at high spatiotemporal resolution using PAT. These results open the way for high-resolution photoacoustic imaging of dynamic biological processes in deep tissues using NIR biosensors and PAT.

Keywords: PAT, photoacoustic microscopy, FRET, biosensor

1. INTRODUCTION

Photoacoustic (PA) tomography (PAT) breaks the optical diffusion limit by acoustically detecting optical absorption contrast.[1] Acoustic waves are orders of magnitude less scattered in biological tissues, providing PAT far better spatial resolution than pure optical imaging in deep tissues (>2 mm).[2, 3] PAT is sensitive to the optical absorption of molecules. It is powerful at detecting both endogenous molecules, such as hemoglobin, cytochromes, DNA/RNA, and melanin, and exogenous probes, such as organic dyes, nanoparticles, and genetically encoded chromophore-containing proteins.[4-18]

The use of genetically encoded bacteriophytochrome (BphP) based near-infrared (NIR) fluorescent proteins (FPs) as contrast molecules in PAT provides the most advanced technology for deep-tissue visualization of molecules and cells at high spatial resolution *in vivo*.[19-22] The BphP-based molecules with absorption peaks at 640–780 nm can be clearly distinguished from hemoglobin and provide the best sensitivity for *in vivo* visualization of cell populations.[23, 24] As chromophores, they incorporate biliverdin, which is abundant in eukaryotic cells as a product of heme metabolism.[25] While PAT with BphP-based molecules is rapidly developing,[19, 20] so far, it has been applied to structural imaging, leaving dynamic molecular processes largely unexplored.

Biological phenomena result from physico-chemical processes of molecular binding, association, conformational change, and catalysis.[26] To visualize dynamic processes, it is necessary to elucidate the functional states of the constituent molecules at different time points. Förster Resonance Energy Transfer (FRET), uniquely sensitive to molecular conformation, association, and separation in the 1–10 nm range, can resolve molecular interactions and conformations.

Naturally, fluorescence microscopy is suited for FRET imaging, which has provided valuable information for biomedical research. Multiphoton microscopy has been widely used for FRET imaging with extended penetration depth.[27-30] However, strong optical scattering in biological tissue impedes high spatial resolution fluorescence imaging of FRET at depths beyond 2 mm. Photoacoustic FRET imaging of dyes[31] and FPs of green fluorescent protein (GFP) family-based biosensors[32] was shown in model systems with purified molecules *in vitro*. However, the use of FRET sensors absorbing in blue/green light range seems to be incompatible with PAT imaging of deep tissues *in vivo*, because the strong optical absorption and scattering from endogenous molecules fundamentally limit blue/green light penetration.[33]

Recently, following the development of spectrally distinct NIR FPs, such as those of (m)iRFP series of proteins,[34-36] genetically encoded NIR FRET biosensors became available. NIR FRET biosensors for GTPase,[36] protein kinases,[36, 37] and calcium dynamics[38] allowed multiplexing with visible FPs for monitoring several processes in single cells.[39] NIR biosensors also can be combined with blue-light controlled optogenetic tools for cross-talk free all-optical control and readout.[39] NIR spectrum of these biosensors is obviously advantageous for their deep and sensitive imaging in living cells and live animals, because of deeper light penetration, less scattering and minimal autofluorescence.[40]

In this work, we applied a genetically encoded NIR FRET biosensor as a probe in PAT. We performed multiscale imaging of biological processes based on FRET *in vivo* for the first time. We investigated two incarnations of PAT, photoacoustic microscopy (PAM) for single cells and photoacoustic computed tomography (PACT) for a deep-seated tumor in the brain, allowing imaging at different scales of spatial resolution and penetration depth.

2. METHODS

To explore NIR FRET with PAT, we developed an improved FRET biosensor for caspase-3 based on miRFP670 donor and iRFP720 acceptor separated by the caspase-3 cleavage site (**Fig. 1A**). We chose to work with the caspase-3 biosensor, because this type of biosensor has been extensively characterized and provides robust responses in single cells. Thus, it perfectly suits the need to test the performance of the novel technology. The optical absorption spectra of miRFP670 and iRFP720 are red-shifted relative to hemoglobin (**Fig. 1B**). The donor miRFP670[35] is spectrally similar to the previously developed dimeric iRFP670[34] that was successfully used in PAT. The miRFP670-iRFP720 FRET pair is characterized by a substantial spectral overlap between the donor fluorescence and acceptor excitation spectra (**Fig. 1C**). The miRFP670-iRFP720 caspase-3 biosensor provided the highest response to cleavage in the suspension of mammalian cells. When excited at 610 nm, the fluorescence changes in the donor channel were almost 2-fold at the peak emission wavelength (**Fig. 1D**). This is higher than that of the previously reported caspase-3 biosensor containing a monomeric miRFP720 acceptor and having the reverse orientation of the donor and the acceptor in a fusion. According to the spectra (**Fig. 1D**) obtained for the HeLa cells stably expressing the miRFP670-iRFP720 biosensor, the donor/FRET ratio was 49%, compared to 34% reported for the biosensor with the miRFP720[36]. Upon excitation, for the miRFP670-iRFP720 caspase-3 biosensor, the generated PA signal consists of the following Eq. (1):

$$PA_1 = P_{DA} + P_A + P_i \quad (1)$$

Here, P_{DA} is the PA signal generated by the donor miRFP670 in the presence of the acceptor iRFP720. P_{DA} is larger than P_D , which is the PA signal generated by the donor in the absence of FRET, because the energy absorbed by the donor is transferred to the acceptor due to FRET[31]. P_A is the direct PA signal generated by the acceptor iRFP720. In this work, we used 610-nm light for FRET imaging. Although 610 nm is away from the donor excitation peak at 643 nm (**Fig. 1B**), a use of 610 nm allows minimizing background by reducing the direct absorption from the acceptor (iRFP720). P_i is the PA signal from endogenous molecules at 610 nm. Once caspase-3 cleaves the -DEVD- linker, miRFP670 and iRFP720 become separated from each other, resulting in no FRET. The PA signals can be expressed as:

$$PA_2 = P_D + P_A + P_i \quad (2)$$

By detecting the PA signal difference between PA_1 and PA_2 , we can photoacoustically monitor changes in FRET.

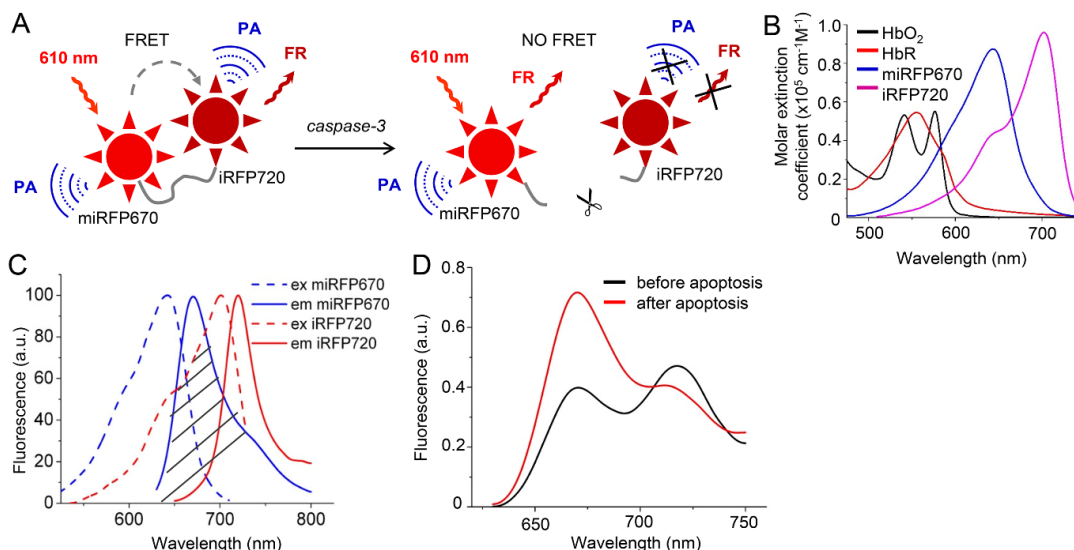


Figure 1. Characterization of a NIR miRFP670-iRFP720 FRET biosensor. (A) Schematic design of FRET miRFP670-iRFP720 caspase-3 biosensor that is activated during apoptosis. PA: photoacoustic signal. FR: fluorescence. (B) Overlay of molar extinction spectra of oxyhemoglobin (HbO₂), deoxyhemoglobin (HbR), miRFP670, and iRFP720. (C) Excitation and emission spectra for miRFP670 and iRFP720. (D) Spectral changes of miRFP670-iRFP720 biosensor.

To obtain miRFP670-iRFP720 caspase-3 biosensor, iRFP720 acceptor was inserted, and the fluorescent proteins miRFP670 and iRFP720 were swapped. The linker between two proteins is GGDEVDGPVAT and the plasmid was obtained from pEGFP-N1 plasmid.

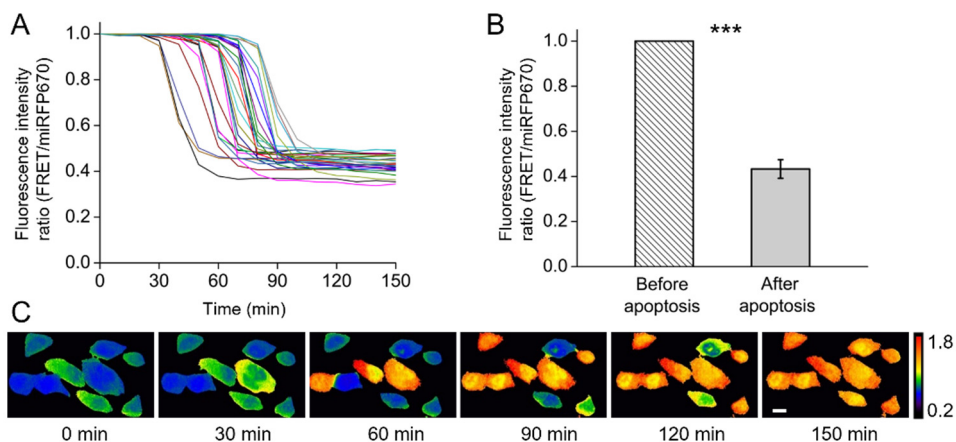


Figure 2. Fluorescence imaging of caspase-3 activity in HeLa cells stably expressing miRFP670-iRFP720 caspase-3 biosensor during STS-induced apoptosis. (A) Kinetics of the fluorescence intensity ratio (FRET/miRFP670) for individual cells undergoing apoptosis. Each line represents one single cell. The images were taken every 10 min. (B) Fluorescence intensity ratio (FRET/miRFP670) before and after STS-induced apoptosis. $n = 30$ cells, error bar, s.d. ***, $p < 0.001$, calculated using a paired Student's t -test. (C) FRET/miRFP670 ratio images at selected time points visualized using intensity pseudocolor. Scale bars, 10 μ m.

First, we tested the miRFP670-iRFP720 biosensor, which was stably expressed in HeLa cells, using fluorescence microscopy. Upon addition of staurosporine (STS) to the cells, caspase-3 activation resulted in biosensor responses (**Fig. 2**). The monitored fluorescence intensity ratio between the FRET (605/30 nm excitation and 725/40 nm emission filters) and the donor (605/30 nm excitation and 667/30 nm emission filters) channels decreased to the minimum of ~40% in 30 min for individual cells and in less than 2 h for a population (**Fig. 2A, B**). Fluorescence images (**Fig. 2C**) illustrate the dynamics in individual cells at subcellular resolution.

As shown in Figure 3A, a pulsed Nd:YAG laser pumps a dye laser to provide 610-nm light for PA excitation. The illumination beam is focused by an objective through a ring-transducer into the mouse ear from the top. The resultant PA waves are detected by a ring-shape ultrasonic transducer. Volumetric imaging is acquired by two-dimensional raster scanning of the mouse ear. The PAM system provides a spatial resolution of ~3–4 μm with a penetration depth of 1 mm.

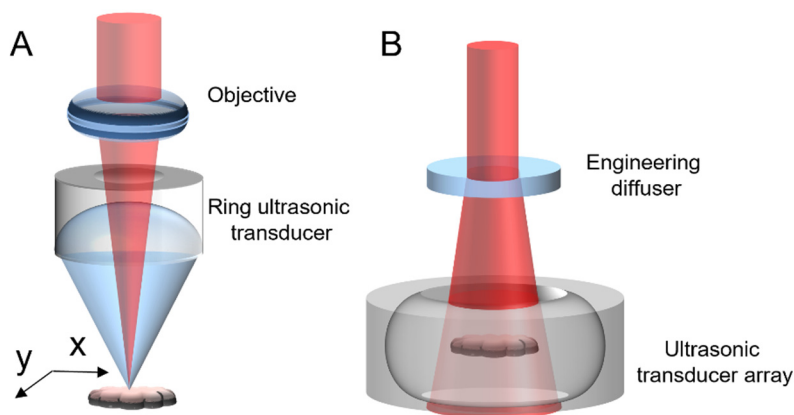


Figure 3. PA imaging setup. (A) Setup of optical-resolution PAM. (B) Setup of PACT.

The PACT system used in this study is shown in Fig. 3B. A lab-made optical parametric oscillator (OPO) laser, pumped by an Nd:YAG laser with a 10-Hz pulse-repetition rate, is used to output 610 nm for PA excitation. The laser beam is first homogenized by an optical diffuser (EDC-5, RPC Photonics) and then illuminated the mouse brain from the top. The maximum light fluence on the skin of the animal is ~10 mJ cm^{-2} , which is well below the American National Standards Institute safety limit. The PA signals are detected by a full-ring ultrasonic transducer array (Imasonic). A lab-made 512-channel preamplifier was directly connected to the ultrasonic transducer array housing. The pre-amplified photoacoustic signals were digitized using a 512-channel data acquisition system. The digitized radio frequency data were first stored in the onboard buffer, then transferred to a computer. The digitized raw data were fed into a half-time dual-speed-of-sound universal back-projection algorithm for image reconstruction.

3. RESULTS

Next, we visualized the FRET sensor expressing cells in the same conditions using optical-resolution PAM (**Fig. 3A**). Under 610-nm illumination, PAM[41-43] revealed the HeLa cells at a spatial resolution of ~3–4 μm . After baseline imaging, STS was added to the cell culture media to induced apoptosis. The kinetics of the PA signals for individual cells (~30 min) and the population (less than 2 h) were similar to those observed in fluorescence measurements (**Fig. 4A**). After 120 min, the PA signals decreased to ~70% of the baseline level (**Fig. 4B**). PAM images also visualize the signal changes in individual HeLa cells during the apoptosis at subcellular resolution (**Fig. 4C**).

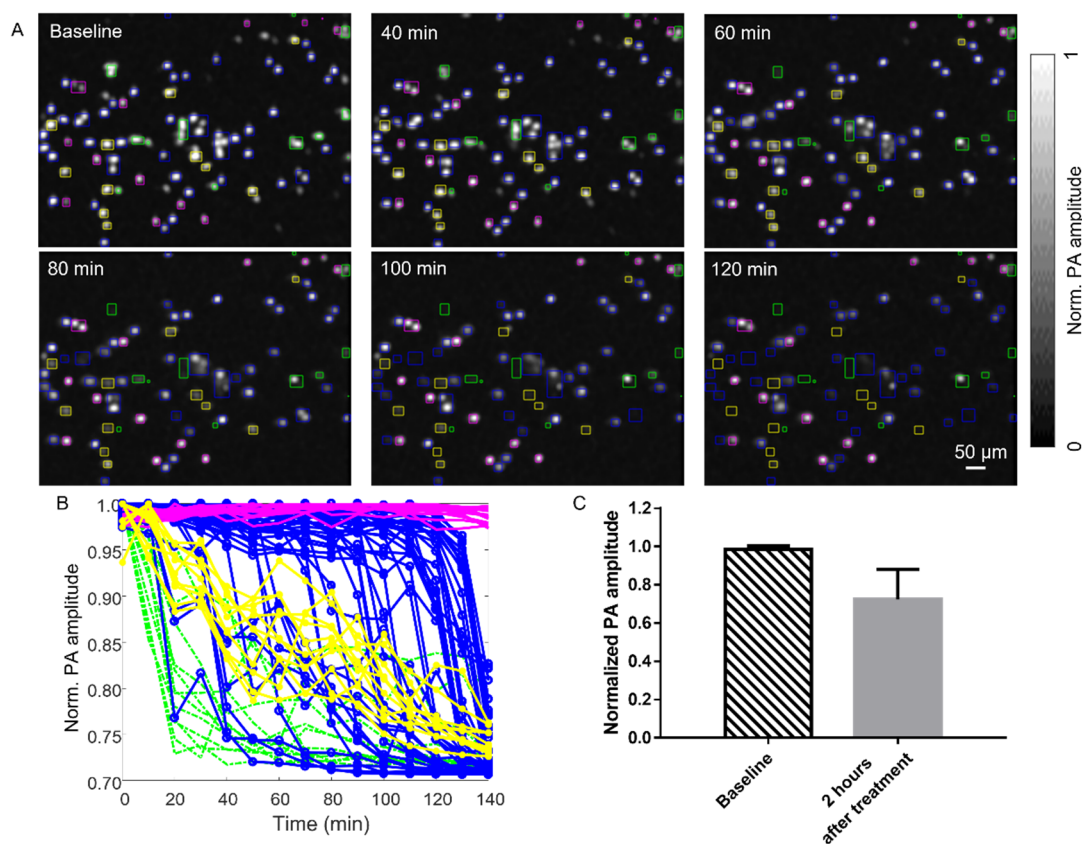


Figure 4. PAM of caspase-3 activity in HeLa cells stably expressing miRFP670-iRFP720 caspase-3 biosensor during STS-induced apoptosis. (A) Representative PAM images of cells at selected time points. (B) PA amplitude changes for individual cells undergoing apoptosis. Each line represents one single cell. (C) PA amplitude before and after STS-induced apoptosis. $n = 40$ cells, error bar, s.d. ***, $p < 0.001$, calculated using a paired Student's *t*-test.

To monitor the FRET processes in deep tissue, we imaged deep-seated tumors in the brain using PACT[7, 44] (Fig. 5A). A tumor was induced in the mouse brain by the injection of 1×10^6 HeLa cells expressing miRFP670-iRFP720 caspase-3 biosensor. Three weeks after injection, the mouse was imaged by PACT. During the *in vivo* experiments, the mouse was mounted onto a holder with the water bag placed on top, and ultrasound gel applied between the scalp and the water bag for ultrasonic coupling. To illuminate the whole brain, a broad laser beam set at 610 nm was used. Throughout the experiments, the scalp was not removed. We first obtained the baseline image of the tumor (3 mm beneath the scalp), we then injected STS (10 μL) in DMSO into the tumor to induce cell apoptosis. The mouse brain was monitored using PACT for ~3 hours. PACT image of a mouse brain 2-h post-injection is shown in Fig. 5B, where the tumor was highlighted by computing the difference from the baseline image. A threshold level of four times the noise level, estimated as the standard deviation of the background signal outside the imaged region, was applied. We selected the three regions for monitoring of the signal changes: the tumor region, the contralateral region, and the biggest vessel in the brain (Fig. 5B). PA signals of the tumor region decreased obviously, while PA signals from non-tumor regions had no significant changes, which indicates the caspase-3 activities inside tumor cells after the STS injection (Fig. 5C, D).

4. DISCUSSION

Here, we demonstrated multiscale PA imaging of FRET biosensors in living cells and live animals for the first time, to the best of our knowledge. We observed that fluorescence imaging of the same NIR biosensor in similar conditions correlated

well with the PA imaging. Specifically, the kinetics of the biosensor responses in individual cells, the variability between cells, and responses in large cell populations were similar. Further, the kinetics of biosensor responses is similar for cell populations observed *in vivo*, showing the PA signals decreased to a plateau in 120-150 min after the STS stimulation. We explored the possibility of applying PAT at different resolutions and penetration depths *in vivo*. In both PAM and PACT, we distinguished vasculature based on hemoglobin contrast from tumor cells expressing the NIR FRET biosensor. PAM has monitored the FRET process at single-cell resolution within 1-mm in depth. PACT has visualized the FRET dynamic in deep seated tumors (>3 mm in depth) at 150- μm spatial resolution. For fluorescence imaging, it is currently not possible to obtain anatomical and functional details at such resolution beyond 1 mm in depth.

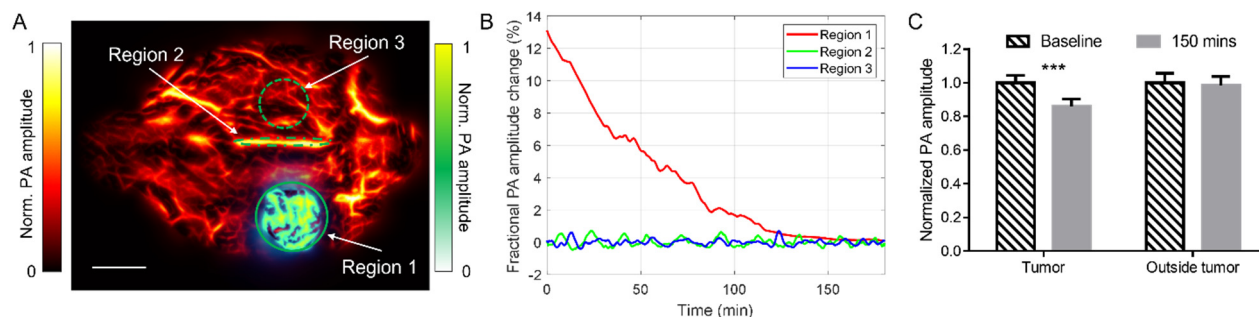


Figure 5. PACT of caspase-3 activity in a mouse brain tumor expressing miRFP670-iRFP720 caspase-3 biosensor during STS-induced apoptosis. (A) PACT image of a mouse brain 2-h post-injection, where the tumor was highlighted by computing the difference from the baseline image. Scale bar, 2 mm. The three regions are the tumor area on the left hemisphere (Region 1), the biggest vessel in the brain (superior sagittal sinus, Region 2), and the region contralateral to the tumor (Region 3). (B) PA signal changes after STS-induced apoptosis. (C) Statistics of PA signals before and after treatment. $n=3$ mice, error bars, s.e.m. ***, $p < 0.001$, calculated using a paired Student's t-test.

REFERENCES

- [1] V. Ntziachristos, "Going deeper than microscopy: the optical imaging frontier in biology," *Nat. Methods*, 7(8), 603-614 (2010).
- [2] V. Ntziachristos, J. Ripoll, L. V. Wang *et al.*, "Looking and listening to light: the evolution of whole-body photonic imaging," *Nature Biotechnology*, 23(3), 313-320 (2005).
- [3] L. V. Wang, and J. Yao, "A practical guide to photoacoustic tomography in the life sciences," *Nature Methods*, 13(8), 627-638 (2016).
- [4] J. Shi, T. T. Wong, Y. He *et al.*, "High-resolution, high-contrast mid-infrared imaging of fresh biological samples with ultraviolet-localized photoacoustic microscopy," *Nature photonics*, 13(9), 609-615 (2019).
- [5] L. Li, J. Xia, G. Li *et al.*, "Label-free photoacoustic tomography of whole mouse brain structures *ex vivo*," *Neurophotonics*, 3(3), 035001 (2016).
- [6] B. Rao, R. Zhang, L. Li *et al.*, "Photoacoustic imaging of voltage responses beyond the optical diffusion limit," *Scientific Reports*, 7, (2017).
- [7] L. Li, L. Zhu, C. Ma *et al.*, "Single-impulse panoramic photoacoustic computed tomography of small-animal whole-body dynamics at high spatiotemporal resolution," *Nature biomedical engineering*, 1(5), 1-11 (2017).

- [8] P. Zhang, L. Li, L. Lin *et al.*, “High-resolution deep functional imaging of the whole mouse brain by photoacoustic computed tomography in vivo,” *Journal of biophotonics*, 11(1), e201700024 (2018).
- [9] Y. Li, L. Li, L. Zhu *et al.*, “Snapshot photoacoustic topography through an ergodic relay for high-throughput imaging of optical absorption,” *Nature Photonics*, 1-7 (2020).
- [10] L. Li, D. Patil, G. Petrucio *et al.*, “Integration of Multitargeted Polymer-Based Contrast Agents with Photoacoustic Computed Tomography: An Imaging Technique to Visualize Breast Cancer Intratumor Heterogeneity,” *ACS Nano*.
- [11] L. Li, Y. Li, Y. Zhang *et al.*, “Snapshot photoacoustic topography through an ergodic relay of optical absorption in vivo,” *Nature Protocols*, 16(5), 2381-2394 (2021).
- [12] J. Shi, T. T. Wong, Y. He *et al.*, “High-resolution high-contrast mid-infrared imaging of fresh biological samples with ultraviolet-localized photoacoustic microscopy (Conference Presentation).” 10878, 1087825.
- [13] J. Yao, A. A. Kaberniuk, L. Li *et al.*, “Reversibly switchable photoacoustic tomography using a genetically encoded near-infrared phytochrome.” 9708, 97082U.
- [14] L. Li, L. Zhu, C. Ma *et al.*, “Imaging small animal whole-body dynamics by single-impulse panoramic photoacoustic computed tomography.” 10064, 100640M.
- [15] Z. Wu, L. Li, Y. Yang *et al.*, “A microrobotic system guided by photoacoustic computed tomography for targeted navigation in intestines in vivo,” *Sci. Robot.*, 4(32), eaax0613 (2019).
- [16] Y. Qu, L. Li, Y. Shen *et al.*, “Dichroism-sensitive photoacoustic computed tomography,” *Optica*, 5(4), 495-501 (2018).
- [17] L. Li, A. A. Shemetov, P. Hu *et al.*, “In vivo photoacoustic multi-contrast imaging and detection of protein interactions using a small near-infrared photochromic protein.” 10878, 1087818.
- [18] P. Zhang, L. Li, L. Lin *et al.*, “In vivo superresolution photoacoustic computed tomography by localization of single dyed droplets,” *Light: Science & Applications*, 8(1), 36 (2019).
- [19] L. Li, A. A. Shemetov, M. Baloban *et al.*, “Small near-infrared photochromic protein for photoacoustic multi-contrast imaging and detection of protein interactions in vivo,” *Nature communications*, 9(1), 1-14 (2018).
- [20] J. Yao, A. A. Kaberniuk, L. Li *et al.*, “Multiscale photoacoustic tomography using reversibly switchable bacterial phytochrome as a near-infrared photochromic probe,” *Nature methods*, 13(1), 67-73 (2016).
- [21] G. S. Filonov, A. Krumholz, J. Xia *et al.*, “Deep-tissue photoacoustic tomography of a genetically encoded near-infrared fluorescent probe,” *Angew Chem Int Ed Engl*, 51(6), 1448-51 (2012).
- [22] L. Li, H.-C. Hsu, V. V. Verkhusha *et al.*, “Multiscale Photoacoustic Tomography of a Genetically Encoded Near-Infrared FRET Biosensor,” *Advanced Science*, 8(21), 2102474 (2021).
- [23] D. M. Shcherbakova, M. Baloban, and V. V. Verkhusha, “Near-infrared fluorescent proteins engineered from bacterial phytochromes,” *Curr Opin Chem Biol*, 27, 52-63 (2015).
- [24] D. Lee, C. Qian, H. Wang *et al.*, “Toward photoswitchable electronic pre-resonance stimulated Raman probes,” *The Journal of Chemical Physics*, 154(13), 135102 (2021).

- [25] D. M. Shcherbakova, A. A. Shemetov, A. A. Kaberniuk *et al.*, “Natural photoreceptors as a source of fluorescent proteins, biosensors, and optogenetic tools,” *Annu Rev Biochem*, 84, 519-50 (2015).
- [26] E. A. Jares-Erijman, and T. M. Jovin, “FRET imaging,” *Nature Biotechnology*, 21(11), 1387-1395 (2003).
- [27] R. N. Day, W. Tao, and K. W. Dunn, “A simple approach for measuring FRET in fluorescent biosensors using two-photon microscopy,” *Nature Protocols*, 11(11), 2066-2080 (2016).
- [28] N. G. Horton, K. Wang, D. Kobat *et al.*, “In vivo three-photon microscopy of subcortical structures within an intact mouse brain,” *Nature photonics*, 7(3), 205-209 (2013).
- [29] T. Wang, D. G. Ouzounov, C. Wu *et al.*, “Three-photon imaging of mouse brain structure and function through the intact skull,” *Nature Methods*, 15(10), 789-792 (2018).
- [30] B. Li, C. Wu, M. Wang *et al.*, “An adaptive excitation source for high-speed multiphoton microscopy,” *Nature Methods*, 17(2), 163-166 (2020).
- [31] Y. Wang, and L. V. Wang, “Forster resonance energy transfer photoacoustic microscopy,” *J Biomed Opt*, 17(8), 086007 (2012).
- [32] Y. Li, A. Forbrich, J. Wu *et al.*, “Engineering Dark Chromoprotein Reporters for Photoacoustic Microscopy and FRET Imaging,” *Scientific Reports*, 6, 22129 (2016).
- [33] L. Li, and L. V. Wang, “Recent Advances in Photoacoustic Tomography,” *BME Frontiers*, 2021, 9823268 (2021).
- [34] D. M. Shcherbakova, and V. V. Verkhusha, “Near-infrared fluorescent proteins for multicolor in vivo imaging,” *Nat Methods*, 10(8), 751-4 (2013).
- [35] D. M. Shcherbakova, M. Baloban, A. V. Emelyanov *et al.*, “Bright monomeric near-infrared fluorescent proteins as tags and biosensors for multiscale imaging,” *Nat Commun*, 7, 12405 (2016).
- [36] D. M. Shcherbakova, N. Cox Cammer, T. M. Huisman *et al.*, “Direct multiplex imaging and optogenetics of Rho GTPases enabled by near-infrared FRET,” *Nat Chem Biol*, 14(6), 591-600 (2018).
- [37] O. S. Oliinyk, A. A. Shemetov, S. Pletnev *et al.*, “Smallest near-infrared fluorescent protein evolved from cyanobacteriochrome as versatile tag for spectral multiplexing,” *Nat Commun*, 10(1), 279 (2019).
- [38] A. A. Shemetov, M. V. Monakhov, Q. Zhang *et al.*, “Bright near-infrared genetically encoded calcium indicator for in vivo imaging,” *Nat Biotechnol*, in press, (2020).
- [39] D. M. Shcherbakova, O. V. Stepanenko, K. K. Turoverov *et al.*, “Near-Infrared Fluorescent Proteins: Multiplexing and Optogenetics across Scales,” *Trends Biotechnol*, 36(12), 1230-1243 (2018).
- [40] R. Weissleder, “A clearer vision for in vivo imaging,” *Nat Biotechnol*, 19(4), 316-7 (2001).
- [41] L. Li, C. Yeh, S. Hu *et al.*, “Fully motorized optical-resolution photoacoustic microscopy,” *Optics letters*, 39(7), 2117-2120 (2014).
- [42] L. Zhu, L. Li, L. Gao *et al.*, “Multiview optical resolution photoacoustic microscopy,” *Optica*, 1(4), 217-222 (2014).

- [43] Y. S. Zhang, J. Yao, C. Zhang *et al.*, "Optical-Resolution Photoacoustic Microscopy for Volumetric and Spectral Analysis of Histological and Immunochemical Samples," *Angewandte Chemie International Edition*, 53(31), 8099-8103 (2014).
- [44] L. Li, L. Zhu, Y. Shen *et al.*, "Multiview Hilbert transformation in full-ring transducer array-based photoacoustic computed tomography," *Journal of biomedical optics*, 22(7), 076017 (2017).